High temperature magnetic studies on $Bi_{1-x}Ca_xFe_{1-y}Ti_yO_{3-\delta}$ nanoparticles: Observation of Hopkinson-like effect above T_N

Pavana S. V. Mocherla, D. Prabhu, M. B. Sahana, Neha Y. Hebalkar, R. Gopalan, M. S. Ramachandra Rao, and C. Sudakar

Citation: Journal of Applied Physics **124**, 073904 (2018); doi: 10.1063/1.5038007
View online: https://doi.org/10.1063/1.5038007
View Table of Contents: http://aip.scitation.org/toc/jap/124/7
Published by the American Institute of Physics

High temperature magnetic studies on $Bi_{1-x}Ca_xFe_{1-y}Ti_yO_{3-\delta}$ nanoparticles: Observation of Hopkinson-like effect above T_N

Pavana S. V. Mocherla,[1] D. Prabhu,[2] M. B. Sahana,[2] Neha Y. Hebalkar,[3] R. Gopalan,[2] M. S. Ramachandra Rao,[4] and C. Sudakar[1,a)]

[1]*Multifunctional Materials Laboratory, Department of Physics, Indian Institute of Technology Madras, Chennai 600036, India*
[2]*Centre for Automotive Energy Materials, International Advanced Research Centre for Powder Metallurgy and New Materials, IITM Research Park, Chennai 600113, India*
[3]*Centre for Nanomaterials, International Advanced Research Centre for Powder Metallurgy and New Materials, Balapur P.O, Hyderabad 500005, India*
[4]*Department of Physics, Nano Functional Materials Technology Centre and Materials Science Research Center, Indian Institute of Technology Madras, Chennai 600036, India*

(Received 30 April 2018; accepted 30 July 2018; published online 21 August 2018)

The magnetic properties of $Bi_{1-x}Ca_xFe_{1-y}Ti_yO_{3-\delta}$ (BCFO: $y = 0$ and BCFTO: $x = y$) nanoparticles are studied across a wide range of temperatures (20 K to 960 K) for different Ca (and Ti) concentrations [$x\ (= y) = 0$, 0.025, 0.05, and 0.1]. X-ray diffraction and electron microscopy revealed the gradual emergence of the orthorhombic phase (P*nma*) with an increase in the Ca^{2+} content in BCFO, contrary to the retention of parent rhombohedral symmetry (*R3c*) in Ca^{2+}-Ti^{4+} co-doped BCFTO. XPS indicates the presence of 3+ valence states for Bi and Fe and under-coordinated defect peaks in O 1*s* spectra. The ordering of oxygen vacancies in BCFO affects the FeO_6 octahedral alignment, resulting in a systematic shift of Fe-O Raman modes. Oxygen vacancies formed due to Ca^{2+} doping in BCFO and the non-magnetic Ti^{4+} ion at the Fe^{3+} site in BCFTO disrupt the spin-cycloid propagation in $BiFeO_3$, largely influencing the magnetic properties. These substitutional changes, in addition to the large surface area, are the sources of net magnetization in these systems. Magnetic hysteresis and field dependent zero field cooled-field cooled curves indicate the combined presence of anti-ferromagnetic and ferromagnetic components in BCFO and BCFTO nanoparticles. High temperature magnetic studies present a clear bifurcation of magnetic Néel transition centered at ~600 K associated with the structural variation in BCFO. A strong anomaly observed at 860 ± 40 K in all the samples suggests a Hopkinson-like effect arising due to sudden loss of anisotropy by the FM component. *Published by AIP Publishing.*
https://doi.org/10.1063/1.5038007

INTRODUCTION

The attempt of achieving better magnetoelectric coupling in multiferroic $BiFeO_3$ (BFO) over the past decade has concurrently resulted in a multitude of studies pertinent to its magnetic properties at room temperature. The cycloidal spin structure in BFO with a repeat distance of 62 nm offers a great deal of interest in tuning the magnetic behavior of the material.[1,2] Intense research by various groups explored this intrinsic long-range structure formed by the canted antiferromagnetic (AFM) alignment of Fe^{3+} spins.[3–6] $BiFeO_3$, a rhombohedrally distorted perovskite belonging to the R*3c* space group, is a type-I multiferroic system where the ferroelectricity arises from the stereochemical activity of the Bi $6s^2$ lone pair with O 2*p* orbitals and the magnetic order is solely from the Fe^{3+} spins residing in an octahedral cage of oxygen ions. $BiFeO_3$ deviates slightly from a regular G-type antiferromagnetic system due to an inherent coupling between the ferroelectric and magnetic order parameters, resulting in canting of neighbouring spins.[7] This canting of spins inhibits complete nullification of magnetic moments; rather, it creates weak net magnetic moments per each unit cell. These weak moments form a spiral structure with a repeat distance of 62 nm propagating along the $[10\bar{1}]$ direction perpendicular to that of the polarization along [111] in $BiFeO_3$. Any disruption to this spin structure below 62 nm could leave out uncompensated magnetic moments in $BiFeO_3$, thereby increasing the magnetization.[8,9] The interest in working on nanostructures of $BiFeO_3$ is driven primarily by this notion. However, nanostructures which are morphologically diversified as cubes,[10] hollow spheres,[11] wires,[12] tubes,[13] core-shells,[14,15] thin films,[16–18] etc., are of different shapes and sizes, where factors such as strain and anisotropy play an important role in tuning the magnetization of the material. Researchers have tried to explain the increase in magnetization with reduction in size using Néel's model of the $1/d$ (where d is the particle size) dependence.[3,19–21] However, size reduction brings along the intricacies of the enhanced surface area, defects, and microstrain which counteract to reduce the magnetization in nanostructures.[9,22–24] Alternative approaches to increase magnetization by doping have also been carried out, yet all the results converge to the point of increased magnetization attributable to the suppressed spin cycloid.[25–30]

a)Author to whom correspondence should be addressed: csudakar@iitm.ac.in. Telephone: +91-44-22574895.

$BiFeO_3$ with a magnetic Néel transition $T_N \sim 643$ K and a ferroelectric Curie transition $T_C \sim 1140$ K can be a potential candidate for room temperature multiferroic applications if the coupling between the magnetic and ferroelectric order parameters can be improved. One possible way of achieving this is by tuning the magnetic order so as to reduce the gap between the magnetic transition and ferroelectric Curie temperatures. Analyzing the magnetic property behaviour at high temperatures, especially around the Néel transition temperature, is essential to have a good understanding in this regard. It is widely reported that A-site substitution affects the magnetic properties of BFO.[25,30,31] In particular, Ca^{2+} at the Bi^{3+} site helps in modulating the magnetic nature of $BiFeO_3$.[29,32–36] However, magnetization observed in doped $BiFeO_3$ nanostructures results from a complex interplay of several crucial parameters, *viz*., particle size and shape, defects induced by doping, associated structural variations, microstrain, anisotropy, and temperature.[4,8,9,23] Zhang *et al*.[37] reported high temperature magnetic studies in Ca doped $BiFeO_3$. They attributed a ferromagnetic transition like anomaly around ~878 K to the Fe^{3+}-O-Fe^{2+} super-exchange interactions. Das and Mandal[38] reported a similar anomaly at a relatively low temperature (< ~873 K) merged up with the actual Néel transition. Gheorghiu *et al*.[39] also reported such an anomaly apart from the Néel transition; however, they attributed this to the magnetic Curie temperature. There are only a few papers discussing this magnetic anomaly at high temperatures in $BiFeO_3$. Also, $BiFeO_3$ is known to be highly prone for defects such as oxygen vacancies and Bi deficiency at high temperatures.[40] The absence of oxygen in the structure leads to a local modification of the AFM alignment between neighbouring Fe^{3+} spins mediated *via* oxygen ions by a super-exchange interaction. In addition, the temperature dependent structural variations that take place in BFO strongly affect the magnetic transition, deciding its proximity to the ferroelectric Curie temperature.[41] The possible influence of defects and related structural changes can also be deciphered from the magnetic behavior at high temperatures. Thus, high temperature magnetic studies give an additional insight into the origin of magnetization in $BiFeO_3$. The analysis of the magnetic variation as a function of temperature, in terms of altered crystallinity, surface structure, and local distortions due to defects, yields in a holistic understanding of the magnetic order in nano-$BiFeO_3$.

In this communication, we report magnetic measurements of Ca^{2+} doped $BiFeO_3$ (BCFO) and Ca-Ti co-doped $BiFeO_3$ (BCFTO) along with pure BFO nanoparticles at different temperatures (20 K to 960 K). The anomalous magnetization peak observed above the magnetic Néel transition of BFO $\sim 860 \pm 40$ K is attributed to the Hopkinson-like effect from the ferromagnetic component, with ferromagnetism arising from the uncompensated moments on nanoparticle surfaces, *independent of the dopant* and the disruption of the spin-cycloid propagation in doped $BiFeO_3$. We also observe a bifurcation and subsequent shift of magnetic Néel's transition in nanoparticles due to the oxygen-vacancy induced structural modulations in Ca^{2+} doped samples.

EXPERIMENTAL

$Bi_{1-x}Ca_xFe_{1-y}Ti_yO_{3-\delta}$ nanoparticles were prepared using sol-gel synthesis which is described in detail elsewhere.[34] $Bi_{1-x}Ca_xFe_{1-y}Ti_yO_{3-\delta}$ represents two systems; in one, only Ca^{2+} is doped at the Bi^{3+} site referred to as BCFO ($Bi_{1-x}Ca_xFeO_{3-\delta-x/2}$; $x \neq 0$ and $y = 0$; $x/2$ is the oxygen vacancy concentration produced by Ca^{2+} doping at the Bi^{3+} site) and the other with Ca^{2+} and Ti^{4+} co-doping at Bi^{3+} and Fe^{3+} sites, respectively, referred to as BCFTO ($x = y$). "δ" is the intrinsic oxygen vacancy concentration present in $BiFeO_3$ nanoparticles. A series of Ca concentrations for $x = 0.025$, 0.05, and 0.1 were doped in BFO to monitor the gradual variations arising from doping. Divalent Ca^{2+} at the Bi^{3+} site produces oxygen vacancies to maintain charge neutrality in BCFO. The BCFO set is compared with Ca^{2+} and Ti^{4+} co-doped system BCFTO for $x = y = 0.025$, 0.05, and 0.1. This system inhibits the formation of oxygen vacancies due to the presence of charge compensating tetravalent Ti^{4+} at the Fe^{3+} site, counter balancing the deficit created by Ca^{2+} at Bi^{3+}. All the characterization is done on the BCFO and BCFTO samples annealed at 650 °C.

X-ray diffraction data were taken using a PANalytical X'pert PRO diffraction system and a Rigaku diffractometer with Cu-kα ($\lambda = 1.5406$ Å). Raman spectra were acquired using a Horiba Jobin Yvon (HR800UV) micro-Raman spectrometer using a 632 nm excitation line from the He-Ne laser averaged over 5 acquisitions each recorded for 60 s. The deconvolution of Raman spectra was carried out using Peak fit P4 software. Differential scanning calorimetry (DSC) was carried out on the as-prepared and annealed samples of pure and doped systems using a TA instruments SDTQ600 thermal analyzer in zero air ambient at a heating rate of 20 °C/min. X-ray photoelectron spectroscopy (XPS) was done using an ESCA+ Omicron Nanotechnology spectrometer on compacted powders in a vacuum of 10^{-9} MPa with an Al $K\alpha$ source (1.48 keV). Thermogravimetry analysis (TGA) and differential scanning calorimetry (DSC) were carried out on as-prepared and annealed samples at a heating rate of 20 °C/min using a TA instruments SDTQ600 thermal analyzer in air. Low temperature and room temperature magnetic hysteresis and zero field cooled (ZFC) and field cooled (FC) curves were measured using a Quantum design SQUID vibrating sample magnetometer in the range +7 T to −7 T. High temperature magnetic measurements were carried out using a vibrating sample magnetometer (EZ9 Microsense Inc., USA) in a field range of +2 T to −2 T. Temperature dependent magnetization was carried out from 300 K to 900 K in Ar ambient with an applied field of 500 Oe.

RESULTS AND DISCUSSION

The structure of BCFO gradually transforms from rhombohedrally distorted perovskite (*R3c*) to a mixed phase of rhombohedral and orthorhombic (*Pnma*) as the doping concentration increases from $x = 0.01$ to 0.1, as discerned from the x-ray diffraction (XRD) studies (Fig. 1). For $x > 0.1$, the cubic structure stabilizes along with an unidentified secondary phase.[34] On the other hand, BCFTO shows a symmetrically broadened double peak till $x = 0.1$, retaining its

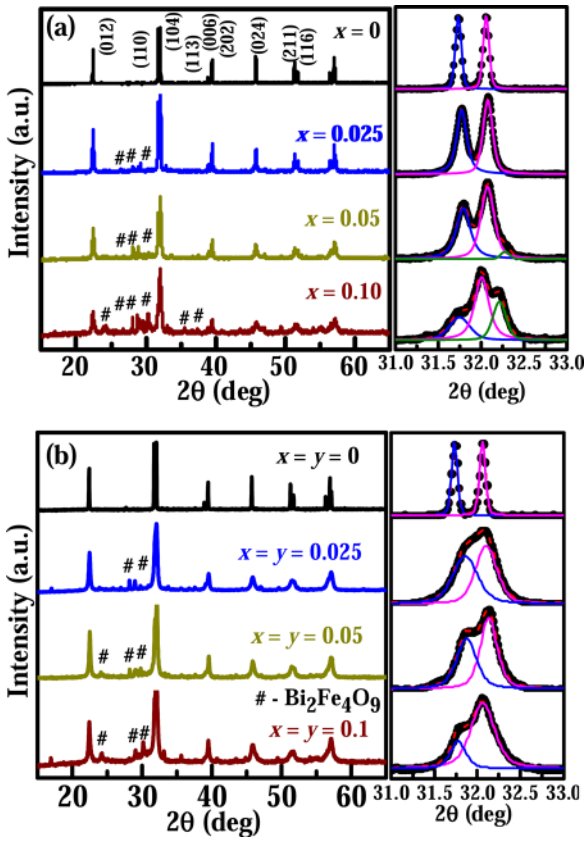

FIG. 1. X-ray diffraction patterns of (a) BCFO ($y=0$) and (b) BCFTO ($x=y$) nanoparticles annealed at 650 °C. The characteristic double peak of rhombohedral $BiFeO_3$ is shown in the panels. # represents minor secondary phase $Bi_2Fe_4O_9$.

rhombohedral structure with no sign of orthorhombic peaks (Fig. 1). However, the relative intensity of these peaks is seen to change with increasing Ca and Ti concentrations, reflecting the structural modifications. The average crystallite size, estimated from various (hkl) reflections using single-peak analysis,[9,42] for BCFO and BCFTO is plotted as a function of doping concentration x (=y) in Fig. 2(a). Compared to the size of BFO annealed at 650 °C, both BCFO and BCFTO show a remarkable size reduction with an increase in x. While the BCFO system shows a gradual decrease, BCFTO shows a swift change down to 36 nm for $x=y=0.025$, with a much flatter decrease than observed in BCFO. The size difference between BCFO and BCFTO for the same doping concentration and annealing temperature must be noted. The presence of Ti^{4+} at the Fe^{3+} site is believed to inhibit the oxygen vacancy formation, keeping the size growth very minimal.[43] We have also estimated the change in lattice parameters and the difference between the characteristic double peak ~32° ($\Delta 2\theta$) in all these samples [Fig. 2(b)]. BCFO shows almost a linear change in the c/a ratio and the $\Delta 2\theta$ variation with x. On the other hand, BCFTO shows an opposite trend in both the plots. All these observations imply that the structural variation in the co-doped system is fundamentally different from that observed in Ca-doped samples. This difference is primarily attributed to the additional perturbations caused by the oxygen vacancies in the Ca doped BCFO system.[34] Generally, phase pure BFO crystallizes around 400 °C. As the annealing temperature is increased, a considerable fraction of $Bi_2Fe_4O_9$ is formed. This is due to the narrow thermodynamic stability of BFO at high temperatures ($T > 600$ °C). It is known that Bi loss at high temperatures is the main source for the formation of Bi deficient phase $Bi_2Fe_4O_9$.[44] Ca^{2+} doping (ionic radius, 100 pm) at the Bi^{3+} site (103 pm) and Ti^{4+} doping (60.5 pm) at the Fe^{3+} site (64.5 pm) affect the crystallization of BFO. The influence of the doping concentration on the crystallization temperature can be understood from the DSC curves where a gradual shift is observed in the crystallization peak of $BiFeO_3$ as the doping concentration increases (Fig. S1 in the supplementary material). Systematic substitution at Bi^{3+} and Fe^{3+} sites enables us to tune the crystallite size and microstrain of BFO nanoparticles. A more detailed version of the Ca^{2+} doping effect on crystallinity is described elsewhere.[34]

Bright field TEM images of BCFO and BCFTO samples showed crystallites with well-defined facets (Fig. 3). The average particle size of these crystallites was found to be in close match to the values estimated from XRD. Localized strain fields created due to the substitutional defects and oxygen vacancies can be inferred from the striking contrast variations within each crystallite. Electron diffraction patterns recorded on oriented crystallites showed additional superlattice-like reflections along $[200]_{pc}$ in BCFO samples. These reflections are attributed to the ordering of oxygen vacancies in BCFO nanocrystals at high temperatures. The size of the supercell formed by oxygen vacancies grows larger with an increase in the Ca concentration. On the

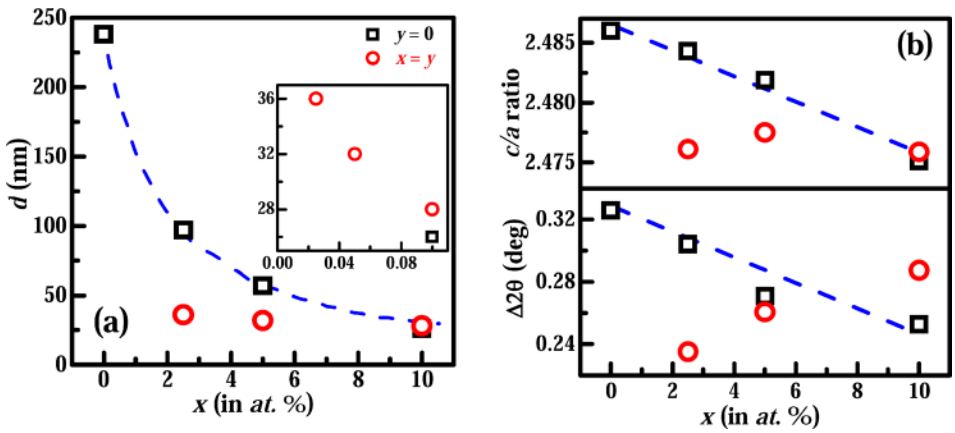

FIG. 2. (a) Average crystallite size of BCFO ($y=0$) and BCFTO ($x=y$) samples plotted as a function of the doping concentration. (b) Top panel shows the change in the c/a ratio and difference between the characteristic double peak $\Delta 2\theta$ in BCFO and BCFTO samples with the doping concentration. The dashed lines in the plots are just guides to the eye.

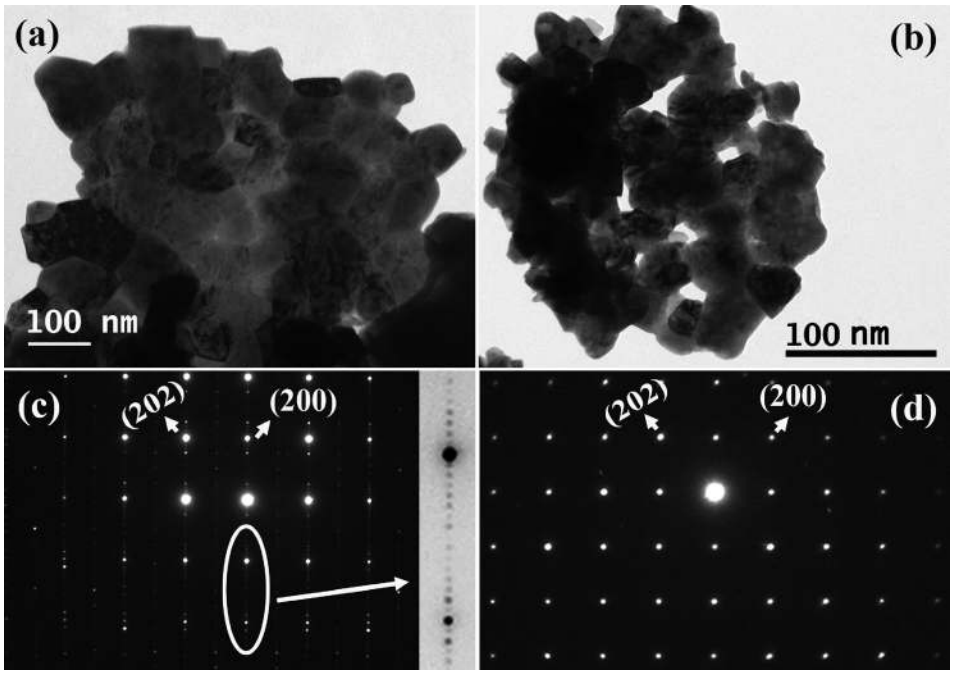

FIG. 3. Representative bright field TEM images of (a) BCFO ($x = 0.05$) and (b) BCFTO ($x = y = 0.05$) samples. All the doped samples show crystallites with well-defined facets and contrast variations. (c) and (d) The electron diffraction patterns recorded on one of the oriented crystallites and indexed in the pseudo-cubic frame of reference. The characteristic four-fold symmetry of $BiFeO_3$ in (c) shows additional reflections along $[200]_{pc}$ due to ordering of oxygen vacancies in the Ca doped sample. BCFTO systems do not show such reflections, confirming the suppression of vacancy formation by Ti^{4+}.

contrary, BCFTO samples showed no ordering in their diffraction patterns in any of the orientations. An extensive microstructural study on these nanoparticles has been presented elsewhere.[34]

Figure 4 shows the XPS core spectra corresponding to Fe 2*p* and O 1*s* levels in BCFO. The positions of satellite peaks in the Fe 2*p* spectra also confirm the 3+ oxidation state of Fe in BCFO samples, suggesting that the charge deficit created by Ca^{2+} doping is compensated by the formation of oxygen vacancies only. There are no other peaks corresponding to the metallic or mixed valence state of cations in the BCFO system. The presence of oxygen vacancies in BCFO samples is also confirmed from the increasing strength of the defect peak ~531.5 eV with the Ca^{2+} content in O 1*s* spectra. A blueshift in the peaks of Bi 4*f* core spectra confirms the substitution of Ca^{2+} at the Bi^{3+} site and the 3+ oxidation state of Bi in the lattice (Fig. S2 and Table ST1 in the supplementary material). X-ray Absorption Near Edge Structure (XANES) studies were also carried out on BCFO and BCFTO systems.[34] Ti is seen to be in the 4+ oxidation state substituted at the Fe^{3+} site in BCFTO. A substantial difference in the oxygen x-ray absorption spectra of BCFO and BCFTO, in combination with electron microscopy studies, confirmed the presence of oxygen vacancies in the BCFO system and the near-stoichiometric composition devoid of vacancies in BCFTO nanoparticles.[34]

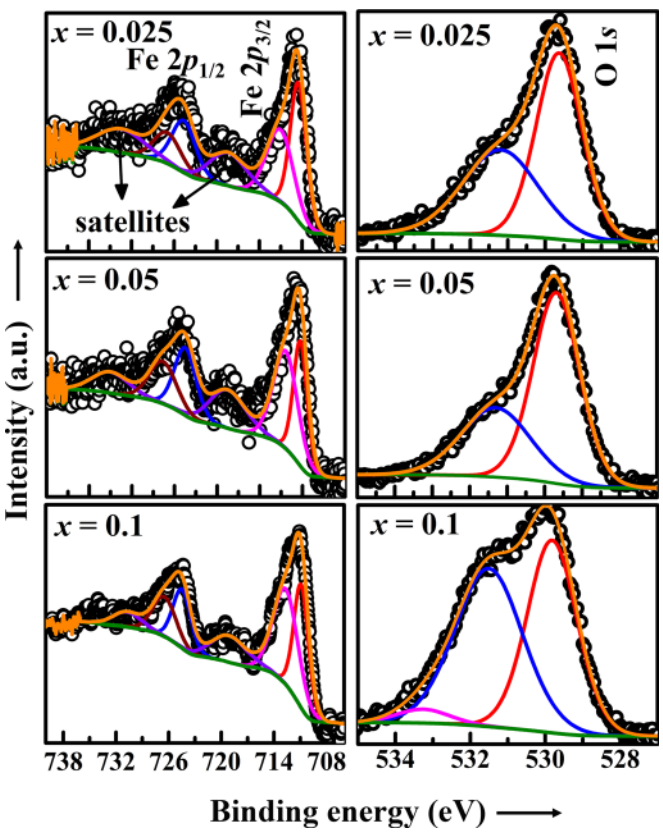

FIG. 4. Core x-ray photoelectron spectra of Fe 2*p* and O 1*s* in BCFO. Data are shown by open symbols with solid lines showing the overall fit for the data. De-convoluted spectral peaks are shown as solid lines. The Shirley background is also shown in the plots.

The Raman spectral signature of BCFO and BCFTO shows characteristic modes of $BiFeO_3$ corresponding to the rhombohedrally distorted perovskite symmetry (Fig. S3 in the supplementary material). Three characteristic modes at ~130, 165, and 268 cm^{-1} which represent the Bi-O bond activity in $BiFeO_3$ show broadening with an increase in the doping concentration.[45] This establishes the effect of crystallinity and size with doping which conforms to the structural variation observed with *x* from XRD data. BFO shows the first strong mode at ~140 cm^{-1} corresponding to the bulk BFO phase as reported previously.[23,46] This strong mode appears between 120 cm^{-1} and 130 cm^{-1} for all the doped samples. This trend in Raman spectra is related to the alternate signature observed in low frequency modes and simultaneous dampening of E(TO) modes in $BiFeO_3$ with reduction in particle size.[23,47] Since these two modes are related to the Bi activity in the material,[48] the redshift observed in BCFO

and BCFTO for different x (=y) could be due to the Ca^{2+} substitution at the Bi^{3+} site and the associated size variation that occurs upon doping. Ca substituted sites lack the stereochemical effect produced by the $6s^2$ lone pair in Bi, thereby changing the overlap of Ca with O $2p$ orbitals, increasing bond lengths, and reducing bond strengths. Peak shifts in Raman modes can also happen when there are strains present in the material.[49] Raman shift increases if the lattice is compressed and decreases if the lattice is under tensile strain. Local changes in the structure driven by the composition and defects could have been the reasons for the observed changes in the Raman signatures.

A substantial influence of doping and strain is also found on Fe-O-Fe bonds along the spin cycloid propagation direction. $BiFeO_3$ exhibits a broad band around 1200 cm^{-1} which comprises three overtones at 900 cm^{-1}, 1100 cm^{-1}, and 1260 cm^{-1} corresponding to the Fe-O fundamental vibrations at ~450 cm^{-1}, 550 cm^{-1}, and 630 cm^{-1}, respectively (Fig. 5).[23,50] Local structural changes, induced by temperature, size, strain, pressure, etc., can be traced from the systematic variation in the position and intensities of these modes comprising the band.[23,51,52] This characteristic band centered at 1200 cm^{-1} is de-convoluted using the Gaussian + Lorentzian profile. The two-phonon band for BCFO and BCFTO samples is shown in Fig. 5 for different x (=y). The mode corresponding to the Fe-O-Fe vibration at ~900 cm^{-1} is

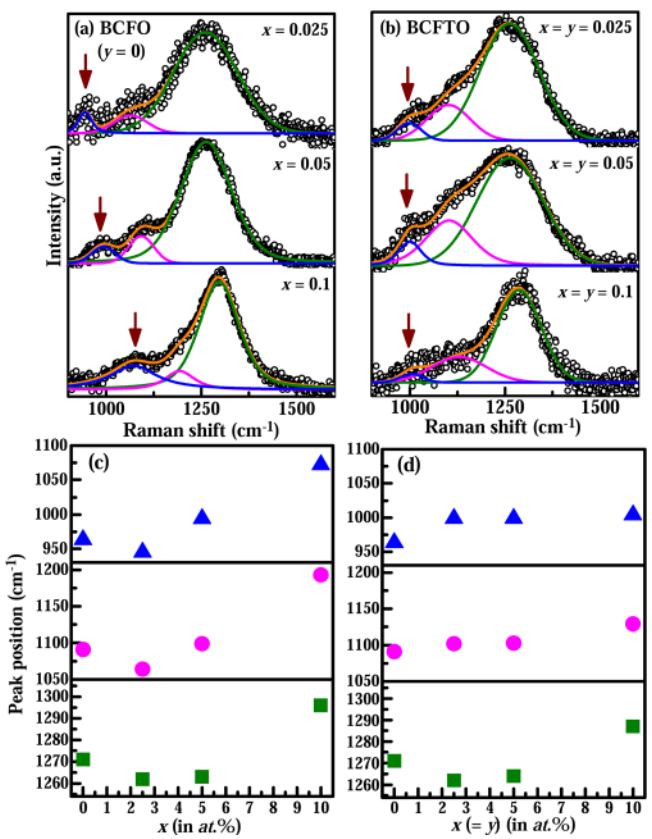

FIG. 5. De-convoluted two-phonon band in (a) BCFO and (b) BCFTO annealed at 650 °C. BCFO shows a clear peak shift (indicated by arrows) with an increase in the Ca concentration, whereas there is no considerable shift in the BCFTO peaks. (c) and (d) The positions of the peaks constituting the two-phonon band as a function of doping concentration for BCFO and BCFTO, respectively.

seen to blue shift with an increase in the Ca^{2+} concentration in BCFO. This mode is connected to the strain in the nanoparticles whose intensity and positions reflect the structural changes in the Fe-O-Fe alignment.[23] On the other hand, the mode is intact and suffers no considerable shift for BCFTO. Positions of constituent peaks of this band are plotted with respect to x in Figs. 5(c) and 5(d). BCFO samples show a large shift in these positions, while BCFTO shows a very minimal shift as compared to pristine BFO. This phenomenon can be understood as follows.

In an ideal case of pure $BiFeO_3$ nanoparticles, spin cycloid termination takes place only on the surface, giving rise to a weak ferromagnetic component besides the core AFM alignment. However, doping at Bi and Fe sites perturbs the spin cycloid within the particle cores in addition to the disruption happening at the surface. In BCFO, the oxygen vacancies produced by Ca^{2+} doping distort the FeO_6 octahedra and affect the Fe-O-Fe antiferromagnetic superexchange. Assuming that the spin cycloid is disturbed in the vicinity of every vacancy produced in the lattice, this scenario results in a cluster-like magnetic ordering confined to very short length scales within each particle. On the other hand in BCFTO, Ti^{4+} being non-magnetic in nature breaks the long range spin structure, giving rise to local uncompensated moments. It was reported that doping the non-magnetic ion at Fe^{3+} in $BiFeO_3$ favors parallel alignment of neighbouring magnetic moments, resulting in enhanced magnetization.[53] The distortion produced in $Fe^{3+}(Ti^{4+})O_6$ octahedra of the BCFTO system is smaller than that caused by oxygen vacancies in $Fe^{3+}O_{6-\delta}$ octahedra of BCFO.[9] A relatively smaller shift in the positions of Raman modes in BCFTO compared to that observed in BCFO is attributed to the degree of distortion in their respective octahedral configuration. Similar magnitudes of peak shifts were observed in pure BFO nanoparticles (<30 nm) with considerable microstrain.[23] Also, BCFTO samples have more surface contribution than BCFO for their smaller size. These intrinsic variations in the spin alignment and the surface contribution for a given doping concentration (and size) decide the net magnetization in these samples. A comprehensive analysis on the sources of magnetization in BCFO and BCFTO is discussed in our previous study.[9] The discussion in the following paragraphs highlight different aspects of the magnetic behaviour in BCFO and BCFTO nanoparticle systems compared to that of pristine BFO.

Room temperature M-H plots of BCFO and BCFTO are shown in Fig. 6. M-H curves of BCFO and BCFTO annealed at 650 °C display a combination of linear antiferromagnetic components overlapped with a ferromagnetic contribution. For all these hysteresis curves, the linear part is subtracted and the ferromagnetic magnetization (M_f) is plotted as a function of the doping concentration [Fig. 6(c)]. The room temperature coercivity of all the samples is also shown as a function of the doping concentration [Fig. 6(d)]. It is observed that M_f in both the cases is of the same order and shows a gradual increase with an increase in "x (=y)." M_f values measured at low temperature (20 K) and room temperature (300 K) are very close to each other, confirming the absence of any magnetic impurities in the samples. This is

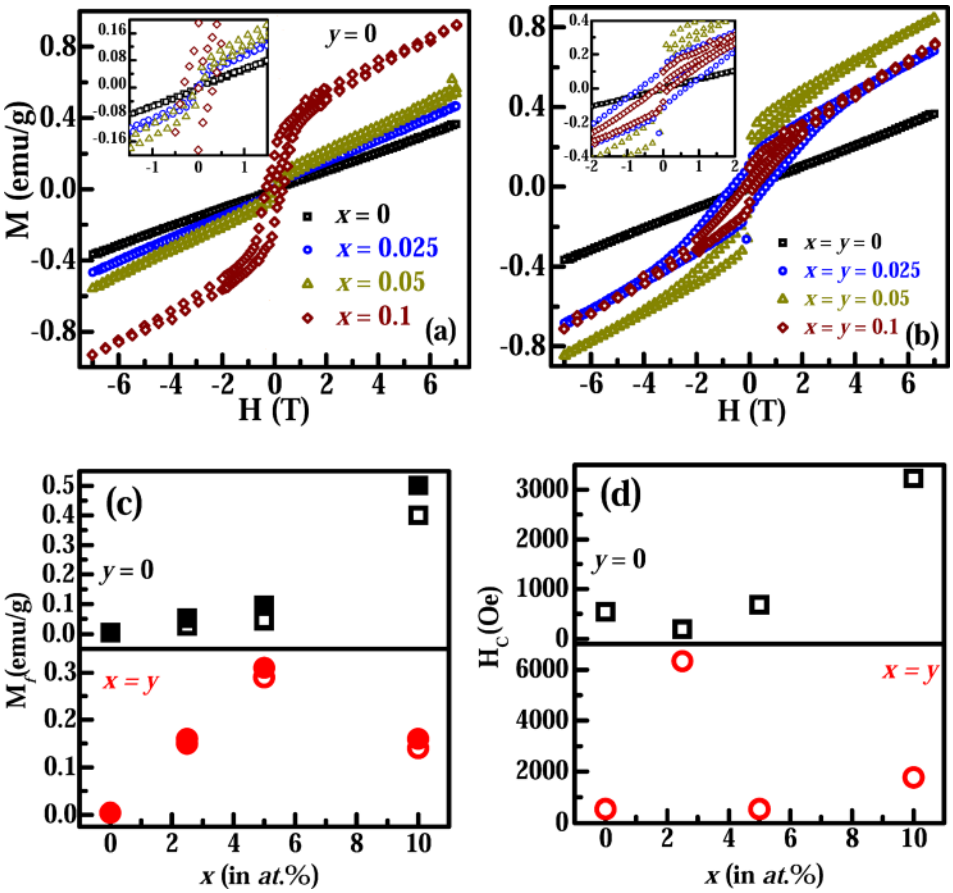

FIG. 6. Room temperature M *vs.* H curves of (a) BCFO and (b) BCFTO samples. Insets show the magnified version of the curves at low applied fields. (c) The variation of ferromagnetic magnetization M_{fm} and (d) room temperature coercivity values of BCFO ($y = 0$) and BCFTO ($x = y$) with respect to the doping concentration in BCFO and BCFTO, respectively.

also in accordance with the Raman spectral studies where no additional modes corresponding to any impure phases were discerned. This implies that any change in the net magnetization is due to the variation of the intrinsic spin structure and not from any magnetic phases.

Another obvious difference between these two systems is the shape of their M-H curves. BCFTO samples display wasp-waisted loops contrary to the predominantly S-shaped loops of BCFO. In general, this pinched loop shape indicates the presence of two sources for magnetic contribution with different coercivities.[54,55] Gupta *et al.*[56] reported a decoupling of antiferromagnetic exchange due to the interaction between the substituent Ce and Fe ions in $BiFeO_3$ thin films. In another study by Yang *et al.*,[57] co-doping of La and Ca has also produced wasp-waisted MH curves in BFO. They have attributed the shape to the cooperative action of Ca^{2+} and La^{3+} ions and uniaxial anisotropy induced by directional ordering of oxygen vacancies.[57] Iorgu *et al.*[58] have reported similar pinched magnetic hysteresis loops in rare-earth doped BFO. Generally, surface anisotropy plays a significant role in determining the shape of hysteresis curves for nanoparticle systems.[59] The surface of nanoparticles hosts several irregularities and point defects, which randomize the spins at room temperature, allowing a quick demagnetization even for small applied fields. BCFTO nanoparticles can have more surface anisotropy than BCFO due to their smaller size.

Figure 7 shows the zero-field cooled (ZFC) and field-cooled (FC) curves of BCFO and BCFTO samples under an applied field of 500 Oe in comparison to the pristine BFO annealed under identical conditions. All the samples show a flat temperature dependent magnetization, confirming the absence of any magnetic impurities or superparamagnetic features. Splitting between ZFC and FC curves usually takes place in systems containing a combination of antiferromagnetic and ferromagnetic components.[6] For pure BFO, we observe a sharp increase in the ZFC-FC data at low temperatures below 30 K. This is due to the small paramagnetic component arising from the surface disorder.[9] Since BFO has larger size than BCFO and BCFTO, it has a relatively smaller surface area compared to the doped systems. Reduction in the surface FM component allows the small paramagnetic component to be revealed at low temperatures. Both BCFO and BCFTO samples show clear irreversibility in the ZFC-FC curves till room temperature, suggesting that these systems contain the FM component at room temperature also. The kinks present at ~250 K correspond to the magnetic Néel transition of the antiferromagnetic $Bi_2Fe_4O_9$ phase. It is a common secondary phase formed during $BiFeO_3$ synthesis involving high temperatures due to Bi volatility from the surface. Nevertheless, this phase does not contribute to the magnetization of $BiFeO_3$ at room temperature because of two main reasons that it is originally an antiferromagnetic system and becomes paramagnetic at 250 K itself.[54,55]

Figure 8 shows field-dependent ZFC-FC curves measured on representative samples using H = 100 Oe, 500 Oe, and 10 kOe. All the samples including pure BFO show a reduced splitting between ZFC and FC curves as the applied magnetic field increases, which is commonly observed in core-shell nanostructures.[15] Also, the temperature at which

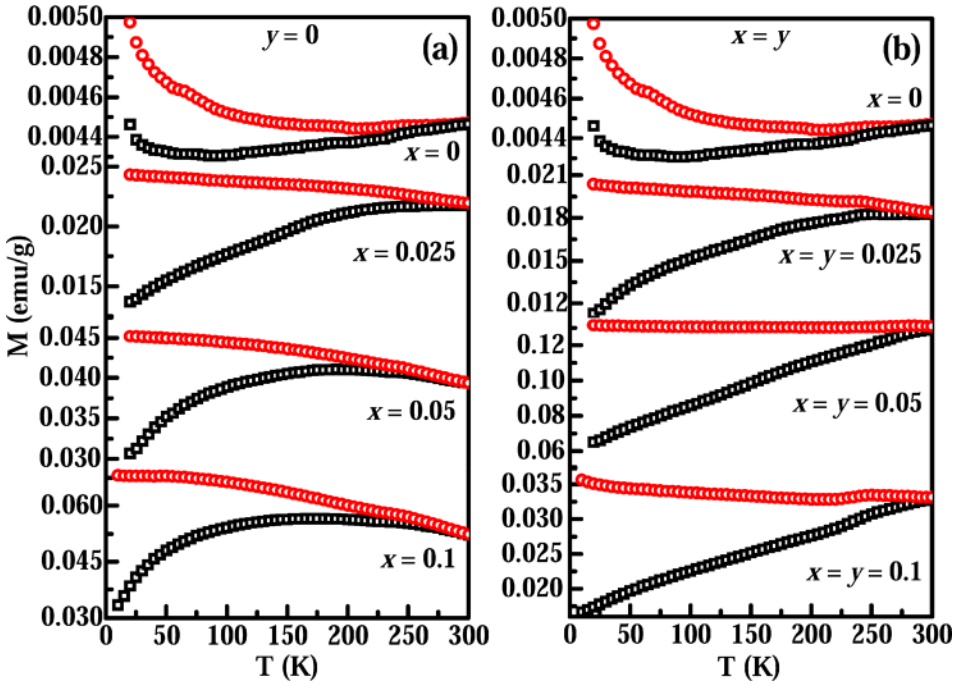

FIG. 7. Zero-field cooled (black squares) and field cooled (red circles) M *vs*. T curves of (a) BCFO and (b) BCFTO samples measured with an applied field of 500 Oe. Both the plots show pure BFO data for comparison.

ZFC and FC data overlap shifts to lower values with increasing H, indicating the nano-like (nanocluster, superparamagnetic, and surface disordered magnetism) features as the origin for the ferromagnetism. Sharp transition observed in ZFC-FC plot (H= 1 T) data of doped samples at ~250 K is related to the secondary phase $Bi_2Fe_4O_9$ as discussed in the x-ray diffraction results. For pure BFO, BCFO05, and BC05FT05 samples, we see another anomaly at ~55 K becoming visible with an increase in the applied field. While Singh *et al.*[60,61] proposed it to be a spin-glass transition in $BiFeO_3$, Vijayanand *et al.*[62] attributed it to some changes in the magnetic domain structure. Huang *et al.*[6] have shown that this cusp is mainly due to the domain pinning effect caused by defects and is observed prominently when a sufficient magnetic field is applied. These MH hysteresis and ZFC-FC studies on both BCFO and BCFTO suggest that a weak ferromagnetic component coexists with the intrinsic antiferromagnetic spin structure. However, we suggest that the origin of the ferromagnetic component in these systems could be fundamentally different.[9] BCFO being a charge deficit system, oxygen vacancies along the Fe-O-Fe chains disrupt the long-range spin-cycloid propagation, thereby creating uncompensated Fe^{3+} spins within the particle cores, in addition to those present on the surface. On the other hand, the spin-cycloid gets interrupted in BCFTO particle cores also, the source of disruption here being Ti^{4+} substituted at Fe^{3+} sites. Hence, it is evident that these systems present a complex mixture of parent antiferromagnetic structures with local weak ferromagnetic moments resulted due to doping and size-related surface changes.[9]

The local structural variations and defect-induced microstrain in BFO nanoparticles also affect the Néel transition temperature.[23] In order to analyze the influence of doping and annealing temperature on the magnetic transition of $BiFeO_3$, we have carried out high temperature magnetization measurements with an applied field of 500 Oe on BFO, BCFO, and BCFTO. The sample preparation for high temperature measurements required dispersion of the powders on a quartz rod base with a temperature-resistant ceramic glue. Excess powder was dusted off to make sure that there

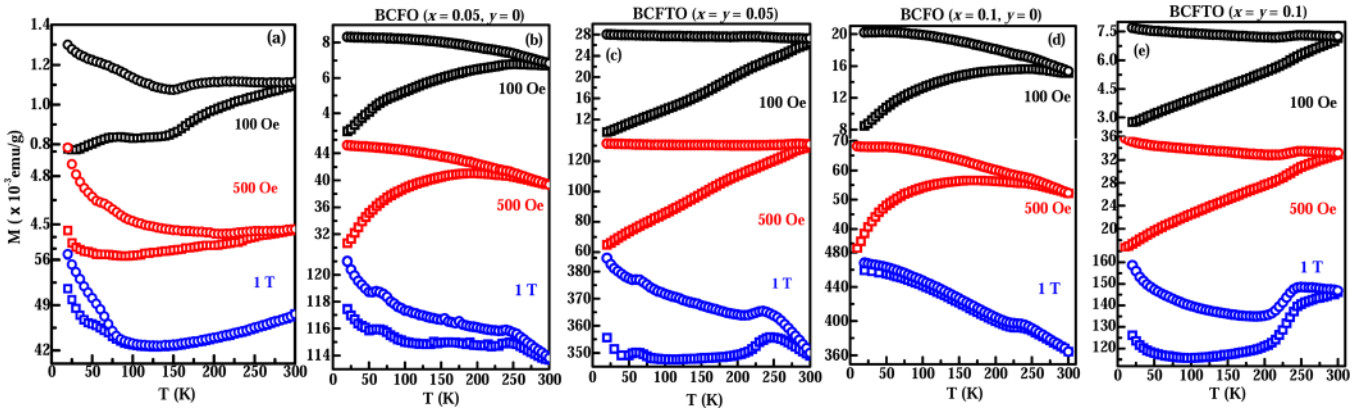

FIG. 8. Field dependent ZFC-FC measurements on selected samples: (a) pure BFO, (b) BCFO05, (c) BC05FT05, (d) BCFO10, and (e) BC10FT10.

are no free particles introduced in the magnetic column. For this reason, the exact mass of the powders used for the high temperature measurements could not be recorded. Hence, all the data of doped samples were normalized to their room temperature magnetization values for an easy comparison. Magnetization in these samples is normalized to the room temperature value (M_{RT}) and plotted as a function of temperature in Fig. 9. BCFO data show two broad humps centered at 600 K. These humps which are closely spaced in $x = 0.025$ widen up gradually with the increasing Ca^{2+} concentration (marked by arrows in Fig. 9). This shows that the magnetic transition of BFO at ~643 K is modified with the structural variations caused by Ca doping.[63] Oxygen vacancies formed due to aliovalent doping disturb the pristine antiferromagnetic alignment of the Fe^{3+} sublattice, thereby influencing the magnetic transition. DSC measurements done on these samples also show gradual evolution of two broad humps with an increase in the Ca content in BCFO, while a single broad transition remains throughout for all the Ca-Ti co-doped BCFTO (Fig. S4 in the supplementary material). This conforms to the gradual structural transformation from rhombohedrally distorted perovskite to the orthorhombic phase around $x = 0.1$ as discerned from x-ray diffraction studies. An increase in T_N of Ca doped BFO has been reported previously by Sardar *et al.*,[29] due to which Ca^{2+} is a preferable dopant at the Bi^{3+} site compared to other divalent cations. This increase in magnetic transition reduces the difference between magnetic and ferroelectric order parameters of BFO, enhancing the magnetoelectric coupling in the multiferroic BFO. On the contrary, BCFTO samples show a single transition around 600 K similar to pure BFO without any considerable shift even with an increase in the doping concentration.

Besides the magnetic transition observed around 600 K, all the samples including pure BFO show another strong feature at 860 ± 40 K. This anomalous peak beyond antiferromagnetic transition was reported previously for bulk samples. Zhang *et al.*[37] also observed a broad feature in the same temperature range ~900 K. They attributed this ferromagnetic-like transition to the Fe^{3+}-O^{2-}-Fe^{2+} interaction. They reported that BFO is likely to produce more oxygen vacancies with an increase in Ca^{2+} which, beyond a particular value, drive Fe^{3+} to Fe^{2+}. Solid solutions of $(1-x)BiFeO_3$–$xBaTiO_3$ have also shown a similar peak in high temperature M vs T curves.[39] These reports have also attributed this feature to the Fe^{3+}-O^{2-}-Fe^{2+} interactions that occur on doping $BaTiO_3$ in the solid solutions.

However, we have a different understanding of the origin of this peak. In pure BFO, especially in the nanoparticle systems, the oxygen vacancies result due to Bi volatility and are usually compensated by driving Fe^{3+} to Fe^{2+}. On the contrary, in BCFO, restoration of charge neutrality in aliovalent Ca^{2+} doped $BiFeO_3$ can take place in two ways. One possibility is that for every pair of Ca^{2+} ions introduced in the lattice, an oxygen vacancy is created apart from the small number of oxygen vacancies invariably present on nanoparticle surfaces. Assuming that there is no oxygen vacancy produced, the other way in which the charge compensation takes place is through a fractional conversion of Fe^{3+} to Fe^{4+}. In an ideal situation, for every Ca^{2+} ion substituted at the Bi^{3+} site, one Fe^{3+} would become Fe^{4+}. XPS and XANES studies have completely ruled out the presence of any Fe^{2+} or Fe^{4+} in our samples, confirming that the charge compensation in BCFO is done solely by oxygen vacancies.[34] Similarly, there are no mixed valence states of Fe in BCFTO samples, also confirming that Ti^{4+} suppressed the formation of oxygen vacancies.[34] Hence, we believe that the strong magnetic feature observed around 900 K is not due to the mixed valence state of Fe and could be from the ferromagnetic interaction of uncompensated spins resulted due to the termination of the spin cycloid. However, these ferromagnetically aligned spins are pinned by the magnetocrystalline and surface anisotropy at room temperature.[59] The appearance of this peak beyond antiferromagnetic transition

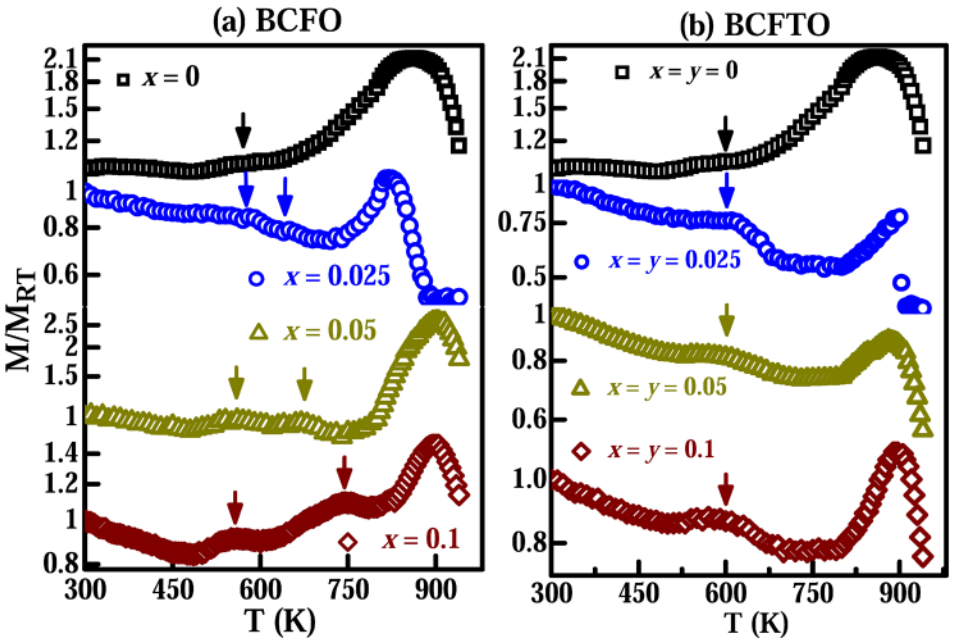

FIG. 9. Magnetization (M) *vs.* temperature (T) curves measured during the heating cycle from 300 K to 940 K with an applied magnetic field of 500 Oe for (a) BCFO and (b) BCFTO. Arrows in the plots indicate the magnetic Néel's transition in each case. For BCFO samples, a clear bifurcation of this transition is observed unlike the broad single peak in BCFTO. The magnetization on the Y-axis has been normalized to the room temperature value. A strong peak at ~870 K is attributed to the Hopkinson-like effect arising from the ferromagnetic component in the samples.

is attributed to the rapid alignment of ferromagnetic spins in the field's direction due to a sudden loss of anisotropy at high temperatures. This is immediately followed by a quick randomization of spins due to continuously increasing temperature. This is very similar to the Hopkinson effect observed in ferromagnetic single domain particles at high temperatures.[64] The presence of a minimum before the Hopkinson peak is also explained in the frame work of the Stoner-Wohlfarth model.[64] The absence of such a strong magnetic feature at high temperature in bulk $BiFeO_3$ confirms that this peak is a nanoproperty.[39] To check for the reversibility of temperature dependent magnetization, the M *vs*. T measurement was done for both heating and cooling cycles (between 300 and 900 K) in inert ambient with an applied magnetic field of 500 Oe for representative samples (only 10%) of BCFO and BCFTO (Fig. 10). Magnetic hysteresis M *vs*. H loops were measured before heating and after cooling cycles [shown only for BFO and BCFO10 samples in Fig. 10(b)]. All the samples show an increase in magnetization after cooling compared to the value before heating. The field cooled M vs T curves do not show this strong anomaly with the magnetic moment higher than the heating curve. This can be due to the spin-reorientation that takes place in the samples when cooled under a magnetic field. TGA-DSC measurements for all the samples were carried out in N_2 and air ambient to understand any chemical variations that can possibly occur at high temperature in oxygen-deficient and oxygen-rich conditions (Fig. S5 in the supplementary material). Pure BFO shows almost a constant profile as the temperature increases in both N_2 and air ambient. BCFO samples (with 5 and 10% Ca) show considerable weight loss in the N_2 environment only beyond 950 K. The weight loss observed here can be due to loss of Bi at high temperatures, primarily evoked by the formation of more oxygen vacancies in reduced ambient. BCFTO samples (with 5 and 10% Ca and Ti) also show a similar trend as that of BCFO. Hence, there is no considerable weight change in any of the samples at ~870 K where the magnetic anomaly is observed. This suggests that this peak in thermomagnetic curves is not due to any compositional or structural variations that take place with temperature. Rather, a competing interaction between the temperature dependent anisotropy (leading to the increase in the magnetization in the FM component at high temperatures) and thermal randomization of ordered spins (leading to the decrease in the magnetization with temperature), similar to the well-known Hopkinson effect, resulted in such a strong peak in the warming cycle of the M vs T measurement.

CONCLUSION

An extensive analysis on the magnetic properties of $Bi_{1-x}Ca_xFe_{1-y}Ti_yO_{3-\delta}$ nanoparticles has been carried out. While divalent Ca^{2+} doping creates oxygen vacancies in the system, Ca-Ti co-doping of equal proportions aid in suppressing the formation of oxygen vacancies. Magnetization increases with an increase in Ca(Ti) doping in both the systems. However, the size difference between these two sets of nanoparticles offers a distinct scenario for the magnetic property origin in these systems. While we ascertain that the magnetic structure in these nanoparticles is a combination of antiferromagnetic and ferromagnetic components, the distribution of ferromagnetic spins is not only merely restricted to the surface like in the case of pure BFO but also dispersed within the particle cores of the doped systems. This cannot be compared to a typical core-shell nanostructure with the AFM core and FM shell; however, the net magnetization will remain to be an aggregate of these sources. Bifurcation of AFM Néel transition in Ca doped samples is attributed to the gradual emergence of the orthorhombic phase with an increase in the Ca content. The ferromagnetically aligned spins in the $Bi_{1-x}Ca_xFe_{1-y}Ti_yO_{3-\delta}$ nanoparticle systems are strongly pinned by the magnetocrystalline and surface anisotropy. The strong anomaly at high temperatures ~870 K observed in all the samples irrespective of doping is

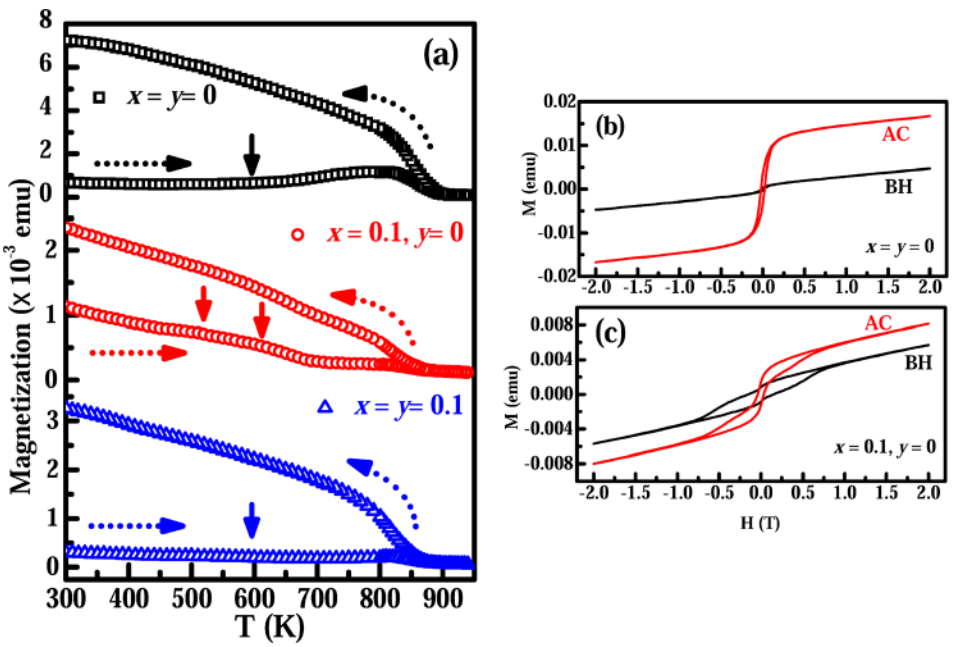

FIG. 10. (a) Magnetization (M) *vs*. temperature (T) curves of representative samples showing both the heating and cooling cycles (marked by dotted arrows) under an applied field of 500 Oe. Vertical arrows on the heating curve indicate the magnetic Néel's transition shown in Fig. 9. The magnetization of the samples increases after cooling. (b) and (c) M *vs*. H curves before heating (BH) and after cooling (AC) the samples pure BFO and BCFO10 ($x = 0.1$), respectively, for M *vs*. T.

due to the sudden loss of anisotropy present between uncompensated FM spins that arise from the termination of the spin cycloid at the defect centers and the surface. Thus, a competing interaction between the temperature-dependent anisotropy and thermal randomization of ordered spins resulted in a Hopkinson-like effect with a strong peak in the warming cycle of the M *vs*. T measurement.

SUPPLEMENTARY MATERIAL

See supplementary material for more details regarding the influence of doping on crystallization temperature, low frequency Raman signature, thermogravimetric changes in reactive and inert ambient at high temperature, oxidation states, and compositional information of Bi, Ca, and Fe in doped systems.

ACKNOWLEDGMENTS

P.S.V.M. and C.S. thank the Central Electron Microscopy Facility. P.S.V.M. acknowledges the research fellowship from UGC. C.S. acknowledges the support from DST-SERB through Grant No. EMR/2016/002785.

The authors declare no competing financial interests.

[1]I. Sosnowska, T. P. Neumaier, and E. Steichele, J. Phys. C **15**(23), 4835 (1982).
[2]H. Feng, J. Magn. Magn. Mater. **322**(13), 1765–1769 (2010).
[3]T.-J. Park, G. C. Papaefthymiou, A. J. Viescas, A. R. Moodenbaugh, and S. S. Wong, Nano Lett. **7**(3), 766–772 (2007).
[4]S. M. Selbach, T. Tybell, M.-A. Einarsrud, and T. Grande, Chem. Mater. **19**(26), 6478–6484 (2007).
[5]A. Jaiswal, R. Das, K. Vivekanand, P. Mary Abraham, S. Adyanthaya, and P. Poddar, J. Phys. Chem. C **114**(5), 2108–2115 (2010).
[6]F. Huang, Z. Wang, X. Lu, J. Zhang, K. Min, W. Lin, R. Ti, T. Xu, J. He, C. Yue, and J. Zhu, Sci. Rep. **3**, 2907 (2013).
[7]G. Catalan and J. F. Scott, Adv. Mater. **21**(24), 2463–2485 (2009).
[8]J. T. Zhang, X. M. Lu, J. Zhou, H. Sun, J. Su, C. C. Ju, F. Z. Huang, and J. S. Zhu, Appl. Phys. Lett. **100**(24), 242413 (2012).
[9]S. V. M. Pavana, M. B. Sahana, R. Gopalan, M. S. R. Rao, B. R. K. Nanda, and C. Sudakar, Mater. Res. Express **4**(10), 106106 (2017).
[10]S. Li, Y.-H. Lin, B.-P. Zhang, Y. Wang, and C.-W. Nan, J. Phys. Chem. C **114**(7), 2903–2908 (2010).
[11]Y. Du, Z. X. Cheng, S. Xue Dou, D. J. Attard, and X. Lin Wang, J. Appl. Phys. **109**(7), 073903 (2011).
[12]B. Liu, B. Hu, and Z. Du, Chem. Commun. **47**(28), 8166–8168 (2011).
[13]J. Wei, D. Xue, and Y. Xu, Scr. Mater. **58**(1), 45–48 (2008).
[14]S. Chauhan, M. Kumar, S. Chhoker, and S. C. Katyal, AIP Conf. Proc. **1591**(1), 521–523 (2014).
[15]S. M. Yusuf, P. K. Manna, M. M. Shirolkar, S. K. Kulkarni, R. Tewari, and G. K. Dey, J. Appl. Phys. **113**(17), 173906 (2013).
[16]N. H. Hong, N. Thu Huong, T.-Y. Kim, S. Goumri-Said, and M. B. Kanoun, J. Phys. Chem. C **119**(25), 14351–14357 (2015).
[17]K. Y. Yun, M. Noda, M. Okuyama, H. Saeki, H. Tabata, and K. Saito, J. Appl. Phys. **96**(6), 3399–3403 (2004).
[18]L. W. Martin, Y.-H. Chu, M. B. Holcomb, M. Huijben, P. Yu, S.-J. Han, D. Lee, S. X. Wang, and R. Ramesh, Nano Lett. **8**(7), 2050–2055 (2008).
[19]R. Mazumder, P. Sujatha Devi, D. Bhattacharya, P. Choudhury, A. Sen, and M. Raja, Appl. Phys. Lett. **91**(6), 062510 (2007).
[20]R. Mazumder, S. Ghosh, P. Mondal, D. Bhattacharya, S. Dasgupta, N. Das, A. Sen, A. K. Tyagi, M. Sivakumar, T. Takami, and H. Ikuta, J. Appl. Phys. **100**(3), 033908 (2006).
[21]L. Neel, *Low Temperature Physics* (Gordan and Breach, London, 1962).
[22]Y. Rui-Peng, L. Si-Xian, F. Xiao-Gong, Q. Ming-Hui, G. Xing-Sen, Z. Min, and L. Jun-Ming, Chin. Phys. B **23**(6), 067102 (2014).
[23]P. S. V. Mocherla, C. Karthik, R. Ubic, M. S. Ramachandra Rao, and C. Sudakar, Appl. Phys. Lett. **105**(13), 132409 (2014).
[24]C. Ederer and N. A. Spaldin, Phys. Rev. B **71**(22), 224103 (2005).
[25]V. A. Khomchenko, D. A. Kiselev, M. Kopcewicz, M. Maglione, V. V. Shvartsman, P. Borisov, W. Kleemann, A. M. L. Lopes, Y. G. Pogorelov, J. P. Araujo, R. M. Rubinger, N. A. Sobolev, J. M. Vieira, and A. L. Kholkin, J. Magn. Magn. Mater. **321**(11), 1692–1698 (2009).
[26]P. Kharel, S. Talebi, B. Ramachandran, A. Dixit, V. M. Naik, M. B. Sahana, C. Sudakar, R. Naik, M. S. R. Rao, and G. Lawes, J. Phys.: Condens. Matter **21**(3), 036001 (2009).
[27]F. Huang, X. Lu, W. Lin, X. Wu, Y. Kan, and J. Zhu, Appl. Phys. Lett. **89**(24), 242914 (2006).
[28]B. Ramachandran, A. Dixit, R. Naik, G. Lawes, and M. S. Ramachandra Rao, J. Appl. Phys. **111**(2), 023910 (2012).
[29]G. Catalan, K. Sardar, N. S. Church, J. F. Scott, R. J. Harrison, and S. A. T. Redfern, Phys. Rev. B **79**(21), 212415 (2009).
[30]B. Bhushan, A. Basumallick, S. K. Bandopadhyay, N. Y. Vasanthacharya, and D. Das, J. Phys. D: Appl. Phys. **42**(6), 065004 (2009).
[31]Z. Zhang, P. Wu, L. Chen, and J. Wang, Appl. Phys. Lett. **96**(1), 012905 (2010).
[32]K. Sardar, J. Hong, G. Catalan, P. K. Biswas, M. R. Lees, R. I. Walton, J. F. Scott, and S. A. T. Redfern, J. Phys.: Condens. Matter **24**(4), 045905 (2012).
[33]V. A. Khomchenko, I. O. Troyanchuk, D. M. Többens, V. Sikolenko, and J. A. Paixão, J. Phys.: Condens. Matter **25**(13), 135902 (2013).
[34]P. V. Mocherla, G. Sanjeev, C. Keun Hwa, M. S. R. Rao, and C. Sudakar, Mater. Res. Express **2**(9), 095012 (2015).
[35]P. Kumar and M. Kar, J. Alloys Compd. **584**, 566–572 (2014).
[36]N. S. Pawan Kumar, A. Srinivasan, and M. Kar, J. Appl. Phys. **117**(19), 194103 (2015).
[37]N. Zhang, J. Su, Z. Y. Liu, Z. M. Fu, X. W. Wang, G. L. Song, and F. G. Chang, J. Appl. Phys. **115**(13), 133912 (2014).
[38]R. Das and K. Mandal, J. Magn. Magn. Mater. **324**(11), 1913–1918 (2012).
[39]F. P. Gheorghiu, A. Ianculescu, P. Postolache, N. Lupu, M. Dobromir, D. Luca, and L. Mitoseriu, J. Alloys Compd. **506**(2), 862–867 (2010).
[40]T. R. Paudel, S. S. Jaswal, and E. Y. Tsymbal, Phys. Rev. B **85**(10), 104409 (2012).
[41]R. Palai, R. S. Katiyar, H. Schmid, P. Tissot, S. J. Clark, J. Robertson, S. A. T. Redfern, G. Catalan, and J. F. Scott, Phys. Rev. B **77**(1), 014110 (2008).
[42]S. V. M. Pavana, *Defect-controlled structure-property correlations in bismuth ferrite nanoparticles* (Indian Institute of Technology Madras, 2016).
[43]Reetu, A. Agarwal, S. Sanghi, and Ashima, J. Appl. Phys. **110**(7), 073909 (2011).
[44]M. Valant, A.-K. Axelsson, and N. Alford, Chem. Mater. **19**(22), 5431–5436 (2007).
[45]R. Haumont, J. Kreisel, P. Bouvier, and F. Hippert, Phys. Rev. B **73**(13), 132101 (2006).
[46]H. Béa, M. Bibes, S. Petit, J. Kreisel, and A. Barthélémy, Philos. Mag. Lett. **87**(3–4), 165–174 (2007).
[47]P. Chen, X. Xu, C. Koenigsmann, A. C. Santulli, S. S. Wong, and J. L. Musfeldt, Nano Lett. **10**(11), 4526–4532 (2010).
[48]P. Hermet, M. Goffinet, J. Kreisel, and P. Ghosez, Phys. Rev. B **75**(22), 220102 (2007).
[49]R. Haumont, J. Kreisel, and P. Bouvier, Phase Transitions **79**(12), 1043–1064 (2006).
[50]R. Palai, H. Schmid, J. F. Scott, and R. S. Katiyar, Phys. Rev. B **81**(6), 064110 (2010).
[51]M. O. Ramirez, M. Krishnamurthi, S. Denev, A. Kumar, S.-Y. Yang, Y.-H. Chu, E. Saiz, J. Seidel, A. P. Pyatakov, A. Bush, D. Viehland, J. Orenstein, R. Ramesh, and V. Gopalan, Appl. Phys. Lett. **92**(2), 022511 (2008).
[52]M. Cazayous, A. Sacuto, D. Lebeugle, and D. Colson, Eur. Phys. J. B **67**(2), 209–212 (2009).
[53]J. Wei, R. Haumont, R. Jarrier, P. Berhtet, and B. Dkhil, Appl. Phys. Lett. **96**(10), 102509 (2010).
[54]S. Godara, N. Sinha, and B. Kumar, Ceram. Int. **42**(1, Part B), 1782–1790 (2016).
[55]S. Gupta, M. Tomar, A. R. James, and V. Gupta, Ferroelectrics **454**(1), 41–46 (2013).
[56]S. Gupta, M. Tomar, and V. Gupta, Ferroelectrics **470**(1), 272–279 (2014).
[57]C. Yang, J.-S. Jiang, C.-M. Wang, and W.-G. Zhang, J. Phys. Chem. Solids **73**(1), 115–119 (2012).
[58]A. I. Iorgu, F. Maxim, C. Matei, L. P. Ferreira, P. Ferreira, M. M. Cruz, and D. Berger, J. Alloys Compd. **629**, 62–68 (2015).

[59]J. M. D. Coey, *Magnetism and Magnetic Materials* (Cambridge University Press, 2010).
[60]M. K. Singh, W. Prellier, M. P. Singh, R. S. Katiyar, and J. F. Scott, Phys. Rev. B **77**(14), 144403 (2008).
[61]M. K. Singh, R. S. Katiyar, W. Prellier, and J. F. Scott, J. Phys.: Condens. Matter **21**(4), 042202 (2009).
[62]S. Vijayanand, M. B. Mahajan, H. S. Potdar, and P. A. Joy, Phys. Rev. B **80**(6), 064423 (2009).
[63]P. Fischer, M. Polomska, I. Sosnowska, and M. Szymanski, J. Phys. C: Solid State Phys. **13**(10), 1931 (1980).
[64]O. Popov and M. Mikhov, J. Magn. Magn. Mater. **82**(1), 29–32 (1989).